HHS Public Access

Author manuscript

Neuroimage. Author manuscript; available in PMC 2017 February 01.

Published in final edited form as:

Neuroimage. 2016 February 1; 126: 208–218. doi:10.1016/j.neuroimage.2015.11.048.

Comparison of glomerular activity patterns by fMRI and wide-field calcium imaging: implications for principles underlying odor mapping

Basavaraju G. Sanganahalli[#,*,¶], **Michelle R. Rebello**[+,%], **Peter Herman**[#,*,¶], **Xenophon Papademetris**[*,¶,¢], **Gordon M. Shepherd**[+], **Justus V. Verhagen**[+,%], and **Fahmeed Hyder**[#,*,¶,¢]

[#]Magnetic Resonance Research Center (MRRC), Yale University, New Haven, Connecticut, USA

[*]Quantitative Neuroscience with Magnetic Resonance (QNMR) Core Center, Yale University, New Haven, Connecticut, USA

[¶]Department of Radiology and Biomedical Imaging, Yale University, New Haven, Connecticut, USA

[¢]Department of Biomedical Engineering, Yale University, New Haven, Connecticut, USA

[+]Department of Neurobiology, Yale University, New Haven, Connecticut, USA

[%]The John B. Pierce Laboratory, New Haven, Connecticut, USA

Abstract

Functional imaging signals arise from distinct metabolic and hemodynamic events at the neuropil, but how these processes are influenced by pre- and post-synaptic activities need to be understood for quantitative interpretation of stimulus-evoked mapping data. The olfactory bulb (OB) glomeruli, spherical neuropil regions with well-defined neuronal circuitry, can provide insights into this issue. Optical calcium-sensitive fluorescent dye imaging ($OICa^{2+}$) reflects dynamics of pre-synaptic input to glomeruli, whereas high-resolution functional magnetic resonance imaging (fMRI) using deoxyhemoglobin contrast reveals neuropil function within the glomerular layer where both pre- and post-synaptic activities contribute. We imaged odor-specific activity patterns of the dorsal OB in the same anesthetized rats with fMRI and $OICa^{2+}$ and then co-registered the respective maps to compare patterns in the same space. Maps by each modality were very reproducible as trial-to-trial patterns for a given odor, overlapping by ~80%. Maps evoked by ethyl butyrate and methyl valerate for a given modality overlapped by ~80%, suggesting activation of similar dorsal glomerular networks by these odors. Comparison of maps generated by both methods for a given odor showed ~70% overlap, indicating similar odor-specific maps by each method. These results suggest that odor-specific glomerular patterns by high-resolution fMRI primarily tracks pre-synaptic input to the OB. Thus combining $OICa^{2+}$ and fMRI lays the

Correspondence to: Basavaraju G. Sanganahalli/[&]Justus V. Verhagen/D. S. Fahmeed Hyder Department of Diagnostic Radiology, 300 Cedar Street, New Haven, CT 06520-8018, USA [&]The John B. Pierce Laboratory, 290 Congress Ave, New Haven, CT 06520-8018, USA basavaraju.ganganna@yale.edu/ jverhagen@jbpierce.org/ fahmeed.hyder@yale.edu.

framework for studies of OB processing over a range of spatiotemporal scales, where $OICa^{2+}$ can feature the fast dynamics of dorsal glomerular clusters and fMRI can map the entire glomerular sheet in the OB.

Keywords

BOLD signal; intrinsic signal; functional hyperemia; glutamate; energetics; olfaction

1. INTRODUCTION

Spatial activity patterns representing odor stimuli in the glomerular layer of the olfactory bulb (OB) were first demonstrated by 2-deoxy-D-glucose (2DG) (Sharp et al., 1975; Stewart et al., 1979), and since then have been confirmed and extended by many other methods (e.g., c-fos: (Guthrie and Gall, 1995); voltage sensitive dyes: (Kauer, 1991), functional magnetic resonance imaging (fMRI) (Poplawsky and Kim, 2014; Schafer et al., 2006; Xu et al., 2003; Yang et al., 1998); calcium imaging (Charpak et al., 2001; Friedrich and Korsching, 1997; Gautam and Verhagen, 2010; Petzold et al., 2008; Wachowiak et al., 2002b); intrinsic imaging: (Gurden et al., 2006; Rubin and Katz, 1999; Wachowiak and Cohen, 2003), and genetically encoded calcium sensor GCaMP (Chaigneau et al., 2007; Wachowiak et al., 2013)). These patterns have given rise to a field of odor mapping, enabling odor coding to be visualized in spatial maps in analogy with mapping in other sensory systems. The patterns are due to differing levels of activity in individual glomeruli, presumably reflecting differing activation of the olfactory receptors in olfactory sensory neurons projecting to the glomeruli. The methods also show systematic changes in the patterns with differing odorant concentrations.

In spite of this consistency in properties, a wide open question in odor mapping is that the different methods do not give consistent patterns across the different methods. There has been no systematic attempt, thus far, to carry out a detailed comparison between any of these mapping methods. This is a critical step for giving confidence in the validity of the different methods in revealing how odor molecules are encoded in the nervous system. It is also critical for determining the advantages and limitations of the different mapping methods.

To fill this need we have, therefore, carried out a study to compare directly two leading methods in OB mapping in vivo. One is wide-field optical calcium imaging ($OICa^{2+}$) set up by calcium loading of the olfactory receptor neurons, which reveals activation of the pre-synaptic axon terminals in the glomeruli of the dorsal OB. The other is fMRI, which reveals activation of both pre- and post-synaptic terminals throughout the olfactory glomerular layer. Exogenous calcium-sensitive dyes coupled to a large Dextran moiety are taken up by olfactory receptor neurons in the nose and are slowly transported to pre-synaptic terminals in glomeruli of the OB, where the pre-synaptic dyes report the input activity of glomeruli (Homma et al., 2009; Jukovskaya et al., 2011; Wachowiak and Cohen, 1998). It is presently thought that the source of the calcium signal is due to transient increases in free cytosolic calcium, directly related to spiking activity of the olfactory receptor neurons (Moreaux and Laurent, 2007; Wachowiak et al., 2013; Yaksi and Friedrich, 2006). In contrast, fMRI has shown that nearly the entire glomerular sheet of the OB is involved with odor coding and

further how these patterns vary as a function of odor parameters (Schafer et al., 2006; Xu et al., 2000; Xu et al., 2003). Unlike OICa^{2+}, fMRI does not provide sufficient temporal resolution to evaluate the individual sniff dynamics (Verhagen et al., 2007). An additional difference is that the source of the signal is very well defined for optical imaging (pre-synaptic in our case of dye-loaded olfactory receptor neurons), but it remains unclear in case of the BOLD response in the OB. The BOLD signal, which is based on endogenous intravascular probe deoxyhemoglobin, reflects an intricate coupling between metabolic and hemodynamic changes that support the neural activities associated with bulk neuropil activity, where both pre- and post-synaptic activities contribute (Hirano et al., 2011; Logothetis et al., 2001; Maandag et al., 2007; Sanganahalli et al., 2009b). We have been able to apply the two methods for the first time to the same animal, imaging first the BOLD signal in the glomeruli layer of an anesthetized rat, and then transferring to imaging OICa^{2+}-labeled olfactory receptor neuron terminals in the glomerular layer of the same rat. Very reproducible fMRI and OICa^{2+} patterns were observed across trials for different odors. Analysis of the correspondence between odor-evoked fMRI of the combined glomerular activity and OICa^{2+} patterns of input activity suggested that input activity plays a dominant role in odor-elicited glomerular patterns reported by BOLD. The results give strong support to using OICa^{2+} to analyze the fast timing of dorsal glomerular clusters, while fMRI can be used to map the entire glomerular sheet.

2. MATERIALS and METHODS

All procedures were performed in accordance with protocols approved by the ethical committee of Yale University School of Medicine Institutional Animal Care and Use Committee (IACUC) and Pierce Animal Care and Use Committee (PACUC). These procedures are in agreement with the National Institutes of Health Guide for the Care and Use of Laboratory Animals. The experiments involved a unique pairing of two olfactory mapping methods in the same animal. Sprague-Dawley rats (250–350 g; n = 5) were used first in the Yale Magnetic Resonance Research Center (MRRC) for high resolution fMRI of the OB at the laminar level. After initial recovery from the anesthetic they were transferred to the John B. Pierce facility where they were allowed to recover fully on a partially heated home cage, which typically required 2–3 days. An additional 3 days were allowed before OlCa^{2+} imaging under anesthesia was performed. The rats were housed individually with ad libitum food and water.

2.1 fMRI experiments

Animal preparation—Rats were anesthetized with urethane (1.5 g/kg, intraperitoneal) to avoid movement artifacts and injected with atropine (0.03 mg/kg, subcutaneous) to avoid mucosal discharge and nasal blockage. Animals under urethane anesthesia were freely breathing and did not require intubation. Eye lubricant (Puralube Vet Ointment, ophthalmic ointment) was applied to each eye to avoid corneal desiccation immediately after anesthetic induction. We continuously monitored the heart rate, breath rate and arterial oxygen saturation level non-invasively using Mouse Ox small animal pulse oximeter (Starr Life Sciences Co., Oakmont PA, USA). The core temperature was measured by rectal probe and maintained by heated water blanket at ~37 °C.

Odor stimulation—Odors were delivered orthonasally through a custom-built olfactometer (Figure 1A) with TTL-controlled solenoid valves (Cole-Parmer, Vernon Hills, IL), synchronized with an MRI acquisition computer. Detailed description of this device is reported elsewhere (Sanganahalli et al., 2009a). The output flow (maintained at 250 mL/min) was connected to a long (~4m) Teflon tube (ID: 2.24 mm) that was led into the scanner room and connected to a nose mask on the rat lying inside the magnet bore. The odor delivery delay due to the long tube was ~4 s. We have taken this time into account during the data processing. The state of each solenoid valve (open/closed) was switched using a relay circuit controlled by CED μ1401 unit (Cambridge Electronic Design Ltd., Cambridge, UK) using Spike2 software. Odor carrier N_2 was mixed with medical grade air flow to control the odor concentration. We used an odor delivery nose cone mounted in the naso-incisor bite bar (Figure 1B), which was an in-line extension of the Teflon tube from the olfactometer to ensure consistent odor delivery to both nares and fitted into the imaging bore of MRI scanner. Odor flowing from the 2.24 mm ID odor tube tends to be laminar and retain this diameter, and is hence likely to miss one or both nares. We modeled the flow in 3 dimensions using SolidWorks 2012–2013 and Flow Simulation 2012 to find the optimal perforated plates to widen the 2.24 mm ID of odor flow to 19.2 mm maintaining the laminar flow of 250 mL/min. This ensured both nares were exposed to the odor flow (Figure 1C). All the odorants were obtained from Sigma-Aldrich (St. Louis, MO, USA) and stored under nitrogen in the dark. To provide a continuous steady-state environment to the nasal mucosa, we applied humidified and preheated (28–30 °C) airflow between odor stimulations. Odor delivery was precisely time-locked to fMRI acquisition in a block design experiment (3-min OFF, 2-min ON, 3-min OFF) and was controlled through Spike2 software. Two different types of odorants were used in these experiments: ethyl butyrate (EB) and methyl valerate (MV). These monomolecular odorants were chosen from the family of odorants whose effects on the OB have been previously characterized (Johnson and Leon, 2000; Uchida et al., 2000; Wachowiak and Cohen, 2001) and which predominantly activate dorsal OB (based on analysis of the database kindly provided by Drs. Johnson and Leon). Since optical imaging is limited to acquiring signals from dorsal OB regions and we aim to compare the spatial activity patterns from both imaging techniques. These two odors were appropriate for the current study design.

Data acquisition—The fMRI data were obtained on a modified 9.4T system interfaced by a Direct Drive console (Agilent Tech, Santa Clara, CA) using an actively shielded gradient coil with 500 mT/m maximum gradient strength and 180 μs rise time (Magnex, UK). A custom-built ^{1}H surface coil (1.4 cm inner diameter) was positioned dorsal to the OB for radio-frequency excitation and reception (Figure 1D). The whole OB was shimmed using in-house B_0 shim method. A Matlab-based (MathWorks, Natick, MA, USA) software package B0DETOX was established in our laboratory to provide largely automated magnetic field processing for spherical harmonic based shimming (Juchem et al., 2014). The static field inhomogeneity was optimized until the half-height line width of water in the shimming voxel was less than 15–20 Hz. Anatomical images were acquired using fast spin-echo sequence (FSEMS) with the imaging parameters of 4.0 s TR, train of 4 echoes, 40 ms effective TE and 12 averages. High resolution T_2 weighted images were acquired in coronal and axial orientations with a matrix size of 128×128, FOV (field of view) of 1.56 cm with

slice thickness of 0.3 mm (122×122 μm^2 in-plane resolution). Five axial slices were imaged from dorsal to ventral position to match with the $OICa^{2+}$ data. The odor-evoked fMRI method was adapted from our earlier work (Kida et al., 2002; Sanganahalli et al., 2009a; Xu et al., 2000). We used gradient echo multi slice (GEMS) with the following parameters: TR = 312 ms; TE = 12 ms; FOV = 1.56×1.56 cm^2; image matrix = 64×64; number of slices = 5; slice thickness = 300 μm (244×244 μm^2 in plane resolution). Sixteen dummy scans were carried out before fMRI data acquisition. Experiments were of a standard block design in which twenty-four scans of five axial slices consisted of nine pure air scans, six odor scans, and nine pure air scans. In all cases, experimental trials were separated by a 30 min period for sufficient recovery (Schafer et al., 2006). We also used several blank (pure air, without odor) control experiments throughout the session to make sure there was no contamination of odors in the odor tube.

2.2 $OICa^{2+}$ experiments

Animal preparation—Methods used in this part of the study closely followed previous work (Gautam et al., 2014). Initially, olfactory receptor neurons in the dorsal recess of the nasal cavity of the rats were loaded bilaterally with dextran-conjugated calcium-sensitive dye (Oregon Green BAPTA 488-1 dextran; Invitrogen, Carlsbad, CA, USA) using a well-established protocol (Wachowiak and Cohen, 2001), adapted for rats (Verhagen et al., 2007). The >10 kD molecular weight of dye ensured that the dye accumulated only in the axonal terminal of the olfactory receptor neuron.

Seven days later and prior to imaging, the dye-infused rats were anesthetized with urethane (1.5 g/kg i.p.) and atropine (0.03 mg/kg), the bone overlying the dorsal surface of the OB was exposed, thinned and coated with cyanoacrylate glue to make the bone transparent (Bozza et al., 2004). The rat's skull was glued to a bar mounted on a stereotaxic holder to stabilize the rat's head. Local anesthetic (2% lidocaine) was applied at all pressure points and incisions. Throughout the surgery and optical recordings the rat's core body temperature was maintained at ~37 °C with a thermostatically controlled heating pad (Omega Engineering Inc, Stamford, CT).

Optical recordings—Optical calcium signals from the dorsal OB were recorded using a CCD camera (Redshirt Imaging LLC, Decatur, GA, USA) with 256×256 pixel resolution, and at a frame rate of 25 Hz, whereas breathing and odor stimulation signals sampled at 200 Hz. This resolution was sufficient to identify single glomeruli at magnifications low enough to image across the dorsal surface of the OB (Figure 1E). The epifluorescence macroscope used was a custom-made tandem-lens type (Ratzlaff and Grinvald, 1991) with 1 × magnification (FOV:6.67×6.67 mm) and high NA (0.85–0.95) CCTV objectives for high SNR. A high power LED (Luxeon LXHL-PE09, Philips Lumileds, San Jose, CA, USA) driven by a linear DC power supply acted as the light source. A custom-made DC amplifier (based on a linear Apex power operational amplifier; Cirrus Logic, Inc., Austin, TX, USA) powered a peltier (Melcor, OT2.0-31-F1) device onto which the LED was glued. The LED-cooling peltier current was proportional to the LED current, yielding a stable illumination. The fluorescence filter set used was BL P01-514 (excitation filter), LP515 (dichroic), and LP530 (emission filter; Semrock, Lake Forest, IL, USA). This system provided fast imaging

capabilities, a large field of view, and low noise. Raw images were converted to images representing the relative change in fluorescence (%ΔF/F) in each pixel and frame after stimulus application. Data analysis was performed using NeuroPlex software (RedShirtImaging LLC, GA, USA), and routines were written in Matlab (MathWorks Inc., Natick MA, USA).

Each imaging session consisted of manually-triggered trials with inter-trial intervals of >3 min. In each trial the same concentration of an odor was presented (Figure 1A) at each of the two 2 s pulses separated by 2.5 s interval, using a custom-built multichannel auto-switching flow dilution olfactometer (Lam et al., 2000) with dedicated lines for each odor to avoid cross-contamination. Two odorants (EB and MV) were presented orthonasally. After each stimulus the nasal cavity was flushed with clean humidified (sparging distilled water) air for one minute. The olfactometer output entered orthogonally into a Teflon odor tube positioned 5 mm rostral to the nose. Odor concentrations are indicated as percentage saturated vapor (% s.v.). Medical-grade air was used to dilute the vapor in the headspace of odor reservoirs to generate the desired concentration. Concentration linearity and accuracy was verified for both imaging modalities using a MiniRae2000 photo-ionization detector. We tested 2–3 concentrations across typically 3–5 trials. We chose a flow rate of 250 mL/min as this was found by Youngentob et al. to be the average flow rate of inspiratory and expiratory sniffing by awake behaving rats (see their Table 2, 1.9–8.9 ml/s) (Youngentob et al., 1987). The Teflon valves (NResearch Inc., NJ, USA) involved in this paradigm were automated by an in-house program (Labview, National Instruments, Austin, TX, USA). All the results are based on the responses to the first odor pulse only unless otherwise stated. Breathing was measured as the movement of the thorax by a piezoelectric strap around the animal's chest as described previously (Gautam and Verhagen, 2012). During each respiration cycle, one sharp upward deflection in the piezoelectric signal occurred during thorax expansion (inspiration). The point of onset of this deflection occurring before and after the stimulus onset time was used as a reference for estimating instantaneous breathing frequency and assessing occurrence of response coupling with breathing cycle.

2.3 Data analysis

fMRI data analysis—Details of data processing have been described earlier (Kida et al., 2002; Schafer et al., 2005). Data were first processed using in-house Matlab (Natick, MA) algorithms. All data sets showing substantial movement artifacts (>25% of a pixel) by center-of-mass analysis were discarded. For each pixel, an average intensity was established for each stimulation period as well as for the flanking rest periods and a Student's t-test generated t values reflecting the odorant-induced activation of each pixel. These t values were then graphically displayed as activation maps of OB responses. Additionally, traces of BOLD activities were generated from maps that show the changes in average slice BOLD intensity, not t value, as a function of time.

OICa^{2+} data analysis—Datasets consisting of optical images of 256×256 pixels sampled at 25 Hz using Neuroplex software on a 12 s trial-by-trial basis. The images were averaged across trials for each stimulus to identify regions of interest (ROI, activated glomeruli). Focal changes in fluorescence in the OB have been shown previously to correspond to

individual glomeruli (Belluscio and Katz, 2001; Bozza et al., 2004). Using the identified ROI we then extracted glomerular response curves. The response magnitudes across each ROI were then measured using this window for each trial as the percent change in fluorescence before and after stimulus onset (% ΔF/F) as reported previously (Gautam and Verhagen, 2012; Verhagen et al., 2007).

fMRI and OICa^{2+} image co-registration—While the fMRI and OICa^{2+} data were recorded in the same animals, the images from each modality had different field-of-view, resolution, and orientation. Moreover with fMRI we had sectioned images whereas with OICa^{2+} we had a projective image (i.e., the 3 dimensional OB was projected onto a 2 dimensional image captured with OICa^{2+}). Therefore the registration of MRI anatomy onto the optical anatomy was necessary to compare the fMRI and OICa^{2+} maps. The registration was based on finding identical anatomical points of the MRI anatomical image and optical anatomical image using the vessel structures on the surface of the OB. Affine transformation matrices were calculated separately for every animal from the selected identical points. Applying the affine transformation matrix to the MRI anatomical image we registered the MRI anatomical image to the optical space, where the identical points have the same coordinates in both images. Since the fMRI images are in the same space as the MRI structural images, albeit with different in-plane resolution, the same affine transformation matrix could be used to co-register the fMRI images to OICa^{2+} images. Smoothing of fMRI data is the result of the co-registration process between fMRI and OICa^{2+} data. Figure 2A is an example of unsmoothed fMRI data. Figure 3 shows that two fMRI slices are needed to recapitulate the OICa^{2+} data in conjunction with a subject-specific affine transformation, which includes interpolation and which has an inherent filtering effect.

The affine transformation matrix solved the problem of different size, resolution and orientation, but due to the curvature of the OB, the initial dorsal fMRI slice depicting the glomerular layer of the dorsal OB covers only the central portion of the projected optical image of the OB. For complete registration of dorsal glomerular sheets we combined together the next fMRI slice. This adjacent fMRI slice contains the glomerular layer at the edge of the dorsal OB, which is not visible at the initial fMRI slice. Replacing the area of the OB (excluding the olfactory nerve layer) of the second slice with the area of the initial fMRI slice, we combined the fMRI slices together to match the dorsal OB in the optical image. We used in house written MATLAB scripts and bioimage suite (bioimagesuite.yale.edu) for the registration process (Joshi et al., 2011).

Comparisons of fMRI and OICa^{2+} activation patterns—While the activation patterns from odor stimulations were qualitatively similar in fMRI and OICa^{2+} recordings, for quantification of similarity we determined the percentage of overlapping areas. In this process we first created binary representations of the odor-activated area, using a threshold to distinguish activated and not-activated areas. For the purpose of discovering the spatial extent of reproducible activated areas above a specific threshold for each modality, we used the following approach. The threshold was selected statistically as a minimum significance level ($p<0.05$) by comparing resting period (before stimulation) vs. stimulated period. When the increase of the signal became significant, the voxel was above the threshold and

considered part of the activation area. In fMRI we considered the voxel activated if the t-value of its Student's t-statistic larger than 1.8, and in OICa^{2+} the same was true if ΔF/F was larger than 0.15%. In addition to the above criteria, we considered the active voxel only if the same voxel was activated in at least with two separate stimulation runs. The contours of these patterns (from the left and right OBs) were presented for better visibility. The percentage of overlaps were calculated as follows

$$\text{Overlap}\,\% = (A_1 \cap A_2 / \min(A_1, A_2)) * 100, \quad \text{Eq. 1}$$

where A_1 and A_2 are the two activated areas we compared. The result could be varied between 0 (i.e., no overlap) and 100% (i.e., complete overlap). A_1 and A_2 were areas from different trials, different odors, min meaning minima of A1 or A2 and different imaging methods.

3. RESULTS

3.1 Temporal dynamics of fMRI and OICa^{2+} responses

We evaluated the temporal dynamics of odor stimulation in fMRI and OICa^{2+} experiments from the same rat (Figure 2). BOLD signal was represented as mean signal intensity from the pixel-wise time series of the selected ROI, where ROI was defined as changes for stimulation by Student's t-test on the left anterior OB (Figure 2A). The magnitude of responses to a given odor across trials with EB and MV were very reproducible across all rats (Figure 2A_i and Figure 2A_{ii}), where the mean BOLD signal changes were 7.7±1.5% for both EB and MV respectively from 40 s after the onset of odor delivery to the end of the stimulation period. Since the fMRI temporal recording was much slower than the OICa^{2+} recording (0.05 Hz vs. 25 Hz), the BOLD intensity changes did not reflect the breathing pattern and odor onset delay (~4 s due to the long tube) was not visible.

While the OICa^{2+} activation maps were similar in appearance for fMRI activation patterns for Rat 1 with EB and MV (Figure 2B), the OICa^{2+} signal intensity changes were much faster. The odor-evoked activity time series (Figure 2B_i and Figure 2B_{ii}) from the dorsal OB during a single trial was normalized by pre-odor background fluorescence levels (ΔF/F), and the difference was referred to the start of the first inhalation after the beginning of odor delivery. This relative change over time was calculated for each identifiable glomerulus in the left anterior OB of Rat 1 ROI (white box) and was subsequently averaged across all activated glomeruli. These calcium responses were highly dynamic. For example, fluorescence increased to 1.4% for Rat 1 0.8 s after the start of EB onset and was followed by a second peak after 1.4 sec (Figure 2B_i). A very similar pattern was shown with MV for Rat 1 (Figure 2B_{ii}). These two peaks were a direct result of breathing activity of the rat, as previously demonstrated (Verhagen et al., 2007), which occurs roughly twice per second in the anesthetized state. The calcium signal maintained this breath-odor modulation as long as the odor was being presented. However the response was delayed by 0.6 sec (15 frames) from the start of the odor delivery process. This response onset delay had two causes. First and foremost, "odor onset" starts with turning of the odor vacuum. The time for the odor to fill the odor tube and reach the nares was estimated roughly at 0.8 sec, based on 4.2 mL/s

flow rate, a 2.6 mL tube volume and 0.6 mL volume between tube face and nares (5 mm tube-nares distance, 12 mm effective tube ID (~80% of actual ID, accounting for friction with the wall and assuming laminar flow)). Second, olfactory receptor neuron activation only occurs after inspiration of the orthonasally presented odor. Across all five rats, the activity of olfactory receptor neuron synaptic terminals peaked at 1.5±0.8% followed by 1.2±0.7 % during EB (Figure 2B$_i$) and 1.3–2.8% followed by 1.4±0.7 % during MV (Figure 2B$_{ii}$). The timing of the fluorescence peaks varied due to different inspiration times and rates across the rats.

3.2 Spatial patterns of fMRI and OICa^{2+} responses

Both MV and EB, which were chosen as odorants because they predominantly activated glomeruli on the dorsal OB (Johnson and Leon, 2000; Uchida et al., 2000; Wachowiak and Cohen, 2001), activated similar regions of the dorsal OB as was apparent by visual inspection (Figure 2). Their maps appeared correlated, yet EB showed more caudal activity in the left caudal dorsal OB and right medial dorsal OB. We co-registered the spatial activity patterns across both imaging modalities for direct comparison. A step-by-step procedure of this registration process is shown in Figure 3 and discussed in Materials and Methods. By applying the affine transformation matrix to relate identical anatomical landmarks in both MRI and optical anatomical images, we co-registered the MRI space to the optical space (Figure 3A). However to capture the projected optical image near the outer edges of the dorsal OB we had to combine two adjacent fMRI slices acquired axially (Figure 3B). Typical examples of odor-induced fMRI activation maps registered to optical space for the same rat are shown in Figure 4. EB and MV induced fMRI t-maps (Figure 4A) and the OICa^{2+} ΔF/F maps (Figure 4B) showed similar spatial activation patterns. We observed identical activation foci of BOLD and OICa^{2+} images to confirm the similar results between different methods. Different clusters of activity maps were observed in both left and right sides of the OB. fMRI activation occurred both medially and laterally on the left side of the OB, whereas predominantly the medial side was activated in the right OB with minor activation in the posterior lateral regions (Figure 4A). OICa^{2+} maps showed symmetrical medial activations in both sides of the OB and also a few clusters in the posterior part of the OB (Figure 4B). We observed fairly similar activation patterns in both imaging techniques across different subjects and odors.

3.3 Comparison of activation areas

Since statistical comparison of activated areas in their own respective modality-specific space, as shown for fMRI (Figure 4A) and OICa^{2+} (Figure 4B) was challenging, we used the percentage of overlapping areas as a measure of comparison between trials, odors, and methods. Subjects were repeatedly exposed to 2 different odorants and the odor-evoked patterns were recorded with fMRI and OICa^{2+}. Both fMRI and OICa^{2+} activation patterns were globally reproducible across subjects, but they also demonstrated local variability. To check the dependence of variability on the strength of the odors we tried different concentrations (5–30%) of odors to see at which odor concentration we could observe reproducible fMRI and OICa^{2+} activations. For the stimulation paradigm used, we obtained very stable BOLD responses at 20% odorant concentration (both for MV and EB), if sufficient time (~30 minutes) was allowed between successive stimulations to avoid

adaptation. Most of the BOLD bulbar activities across rats showed the greatest responsiveness along medial and lateral surfaces. However, there were some variations both in the distribution of activity within these zones and in the extent to which these activations extended onto the dorsal and ventral surfaces (activations from ventral slices are not shown here). We also observed concentration dependent (5–20%) odor evoked calcium responses (data not shown) and found that a 10% concentration of MV and EB during a 2 s exposure showed stable responses, and which were not over-stimulated. Since there was negligible difference between $OICa^{2+}$ maps for 10% and 20% odorant concentrations, we used maps with 10% odorant concentration to avoid ORN habituation and thereby allowing multiple trial/odor experiments per session. Since the anatomical origin, timing and spatial resolution of the BOLD and $OICa^{2+}$ pattern were different, we statistically selected the thresholds for these patterns. For the BOLD Student's t-maps we selected t=2 as the threshold, which described all of the significantly activated areas (Figure 4A). For $OICa^{2+}$ $\Delta F/F$ map we selected 0.15 % $\Delta F/F$ change (similar to the $p<0.05$ significance level used with fMRI) as activation threshold (Figure 4B), based on earlier glomerular recruitment analyses (Gautam et al., 2014). Every pixel with a value above the threshold was considered part of the activation area in a binary manner to make comparisons of map overlaps between trials, odors, and methods.

3.3.1 Description of activation areas for comparison—Figure 4 shows the OB responses of a subject exposed to EB and MV in three repeated stimulations (Trial 1 to Trial 3) for each odorant. While similar regions were activated across trials, there were notable differences between trials both with fMRI and $OICa^{2+}$. The overlaps between at least 2 trials are shown as color-coded maps in Figure 4C and Figure 4D for fMRI and $OICa^{2+}$, respectively. From these color-coded maps of overlap between two trials (e.g., trial 1 and 3, or trial 1 and 2, or trial 2 and 3) contour maps were obtained to demonstrate the spatial extent of activity patterns that were reproducible (Figure 4E and Figure 4F). In this manner the overlap between two contour maps across trials (Figure 5), odors (Figure 6), and methods (Figure 7) was estimated.

3.3.2 Trail-to-trial comparison of activations—We observed great trial-to-trial reproducibility with both imaging methods. Figure 5 shows the trial-to-trial comparisons of OB responses within fMRI and $OICa^{2+}$ patterns for each odor. Figure 5A shows an example of a subject exposed to MV (same rat as in Figure 4) with fMRI and $OICa^{2+}$. We calculated the degree of trial-to-trial overlap on the left, right, and whole OB using Eq. 1. Inter-trial overlaps in left, right, and whole OB with MV, across all 5 rats, were ~80% for both fMRI and $OICa^{2+}$ (Figure 5B). Inter-trial overlaps in left, right, and whole OB with EB were approximately the same for both fMRI and $OICa^{2+}$ (Figure 5B). While statistically not significant, the BOLD patterns with MV in the right OB was smaller than in the left OB, which was also observed with $OICa^{2+}$ patterns with MV. The only statistical differences were shown between BOLD with MV in right OB and $OICa^{2+}$ with EB in left OB ($p=0.003$) and between BOLD with MV in right OB and $OICa^{2+}$ with MV in left OB ($p=0.007$).

3.3.3 Odor-to-odor comparison of activations—Odor-to-odor comparisons (for a given method) showed significant overlap. Figure 6 shows the odor-to-odor comparisons of

OB responses with EB and MV. Figure 6A shows an example of a subject exposed to EB and MV from the same rat as in Figure 4. We calculated the degree of odor-to-odor overlap on the left, right, and whole OB using Eq. 1. Inter-odor overlaps in left, right, and whole OB, across all 5 rats, were ~80% for both fMRI and OICa^{2+} (Figure 6B). While fMRI odor comparisons were approximately the same on the left and right OB ($p=0.364$), OICa^{2+} odor comparisons showed statistical differences between left and right OB ($p=0.028$).

3.3.4 Method-to-method comparison of activations—Method-to-method comparison showed substantial overlap, indicating odor-induced neural and hemodynamic changes were well mapped. Figure 7 shows the method-to-method comparisons of OB responses between fMRI and OICa^{2+}. Figure 7A shows an example of a subject exposed to EB or MV and recorded by fMRI and OICa^{2+} (same rat as in Figure 4). We calculated the degree of method-to-method overlap on the left, right, and whole OB using Eq. 1. Inter-method overlaps in left, right, and whole OB, across all 5 rats, were ~70% for both EB and MV (Figure 7B). While EB stimulation comparison showed approximately the same values on the left and right OB ($p=0.718$), MV stimulation comparison showed statistical differences between left and right OB ($p=0.040$).

4. DISCUSSION

We correlated fMRI and OICa^{2+} in the OB, a structure that is uniquely suited for this comparison due to its marked and accessible laminar anatomy, to find distinct properties of the two types of imaging signals in OB response to orthonasal odor stimulation. Since it remains unknown how the results reported by these two techniques relate to one another, we sought to combine application of these two complementary techniques on the same subjects to test if odor-induced activation maps differ significantly between both methods. To improve the functional understanding of odor-evoked glomerular activity patterns revealed by BOLD signal and to relate how the input activities of glomeruli reflected by OICa^{2+} relate to bulk neuropil activity of fMRI, we imaged the same rats with fMRI first followed by OICa^{2+}. The hybrid method for sequential recordings of fMRI and OICa^{2+} provides opportunities for directly linking BOLD responses to underlying neural activity. Our results revealed similar and distinct properties of the two types of signals. Very reproducible **fMRI** and OICa^{2+} patterns were observed across trials for different odors. Excellent correspondence between odor-evoked fMRI and OICa^{2+} patterns of input activity suggests that input activity is a dominant part of neuropil activity within glomeruli. Comparison of odor activity maps generated by both methods for a given odor showed ~70% overlap, indicating similar odor-specific maps by each method. These results suggest that odor-specific glomerular patterns by high-resolution fMRI primarily tracks pre-synaptic input to the OB as revealed by OICa^{2+}. Thus OICa^{2+} may be used to feature the fast timing of dorsal glomerular clusters, while fMRI may be used to map the entire glomerular sheet, specifically for odors that activate lateral and ventral glomeruli.

4.1 Comparison of current results with previous studies

Multimodal imaging techniques have been used extensively to study olfactory sensory processing. These techniques include 2-deoxyglucose autoradiography (Sharp et al., 1975),

c-fos expression (Guthrie et al., 1995), electrophysiology (Li et al., 2014), optical imaging of voltage-sensitive dyes (Charpak et al., 2001) or intrinsic signals (Wachowiak and Cohen, 2003), synthetic calcium dyes (Gautam and Verhagen, 2012; Verhagen et al., 2007), genetically encoded calcium sensor GCaMP (Wachowiak et al., 2013), fMRI (Yang et al., 1998), positron emission tomography (PET) (Qureshy et al., 2000), and functional ultrasound (Osmanski et al., 2014). While each of these techniques provides unique information, each has several limitations that affect data interpretation. fMRI studies in OB have laid the groundwork for in vivo odor mapping with high reproducibility (Kida et al., 2002; Schafer et al., 2005; Xu et al., 2000; Xu et al., 2003; Yang et al., 1998). However most previous fMRI studies used coronal imaging of entire OB responses. OICa^{2+} has revealed fine spatiotemporal glomerular patterns of the dorsal part of the OB (Charpak et al., 2001; Petzold et al., 2008; Wachowiak et al., 2002a). An additional difference is that the source of the signal can be very well defined for optical imaging (e.g., pre-synaptic with OICa^{2+}), but remains unclear in case of the BOLD signal of the OB.

Our results showed correspondence between odor-evoked fMRI and OICa^{2+} maps, confirming a relationship between bulk neuropil and pre-synaptic activities (Supplementary Figure 1). This suggests that the input activity in glomeruli dominates glomerular functions. These results are in good agreement with an energy budget of glomerular activity, as the activated state is dominated by energy demands of action potential propagation in afferent olfactory sensory neurons and their synaptic input to dendritic tufts, whereas subsequent dendritic potentials and dendrodendritic transmission contribute minimal energy costs (Nawroth et al., 2007).

4.2 Methodological considerations and limitations

Differences between the two imaging approaches were minimized, e.g., we used the same subject and anesthetic dose for both imaging modalities. However imaging was performed on different days. Physiology plays a crucial role in obtaining reproducible data in both imaging modalities. In an effort to approximate normal physiology, particularly respiration, our fMRI and OICa^{2+} protocols made use of freely breathing subjects noninvasively monitored for movement and under urethane anesthesia. For fMRI we continuously monitored heart rate, breath rate, pulse distention, breath distention, and arterial oxygen saturation using an MRI compatible pulse oximeter. The disadvantage of this approach is that physiological parameters such as blood pH, pCO2, and pO2 which are known to affect the BOLD signal were not controlled via mechanical ventilation, which would have been hard to implement across multiple imaging sessions spanning over several days and given the need for surgical intervention to the rat. Differences in the level of anesthesia may also have played a role in signal differences, even though subjects were maintained under chronic deeply anesthetized state. To the extent that anesthesia and systemic physiology were likely to affect the BOLD signal in a global manner, these effects were partially avoided by thresholding the activation maps. Similar care was taken to monitor animal breathing and physiology during OICa^{2+} experiments. Significant technical advances would be needed to obtain OICa^{2+} signals simultaneously with fMRI data.

The method we used to define similarity by calculating overlapping activation areas depends on the threshold value chosen. While the selected threshold was defined by minimal significance or noise level (i.e., $p<0.05$ in fMRI and 0.15 % $\Delta F/F$ in $OICa^{2+}$), it is clear that selecting a higher threshold would reduce the activated area as well as the areas overlapping between trials, odors, or methods. However, we found that our binary comparison method is rather robust to such threshold changes (data not shown), unless thresholds were extreme. We selected a low, but similar statistical threshold, to ensure that our reproducible activation results were comparable given the technical limitations of each technique to follow response localization problems. First, the convex surface of the OB causes distortion of the projective $OICa^{2+}$ response location at the edges. Second, the registration of BOLD images has a blurring effect on the precise location of the BOLD response. A lower threshold avoids ignoring the signal amplitudes that were reduced by these two inescapable factors. We also point out that, although we used multiple slices in the fMRI data to depict the dorsal glomerular sheet, it remains possible that some residual activities from the olfactory nerve layer are present in the BOLD data as the dorsal glomerular sheet is not perfectly parallel to the axial slices in the fMRI data. In some trials the odor induced activation patterns were somewhat different between the left and right OBs. This may be due to the nasal cycle which imposes an asymmetric airflow through the two nasal passages. Further, unilateral obstructions may spontaneous occur during recording sessions because of nasal congestion, although atropine was infused regularly to avoid this. Partial obstruction of a unilateral airway occurs even in normal physiological conditions and has been reported as part of the normal nasal cycle (Bojsen-Moller and Fahrenkrug, 1971; Kikuta et al., 2008). In addition, calcium sensitive dye has to be injected separately into each side of the nasal cavity. Dye labeling is unlikely to be identical between the olfactory receptor neurons in the two dorsal recesses, resulting in slightly different resting fluorescence patterns across the two dorsal OBs. To counteract the impact thereof on activity maps, the odor-evoked changes in fluorescence are normalized to the resting levels at each pixel, but this may not be completely effective. Hence, differences between $OICa^{2+}$ patterns of the two OBs may be due to static asymmetry of dye labeling as well as due to more dynamic asymmetry in nasal flow. Different odor exposure times across methods can lead to different activation patterns because of absorption of odorants to olfactory epithelium. The glomerular dynamics that spread from posterior to anterior during each sniff at a 100–200 ms time scale. We considered this for our analyses, and hence both fMRI and $OICa^{2+}$ responses were integrated over time to avoid this potential pitfall as it included the response across the entire sniff cycle (for $OICa^{2+}$) or multiple sniff cycles (for fMRI). These odors, as mapped by both imaging techniques over several trials, showed that the dorsal glomeruli respond very similarly. This finding does not extend to the majority of glomeruli (i.e., lateral and ventral glomeruli), which cannot be mapped by $OICa^{2+}$ and thus compared by fMRI. As can be seen in Figure 2, the dynamic of each modality in the same regions of the dorsal glomerular sheet are quite similar across rats. Thus we believe that unless all glomeruli are mapped simultaneously, and which has been done before by fMRI and 2DG in past studies, the odor differences cannot be fully compared to the perception of these odors.

4.3 BOLD versus pre-synaptic calcium responses

Our results showed similar activated areas for each odor under both imaging modalities in the same subjects, confirming a relationship between functional hyperemia and input activity to glomeruli (Figures 4–7). However the relationship is quite complex (Supplementary Figure 1). With odorant stimulation, fMRI (hyperemic) and OICa^{2+} (pre-synaptic) were positively correlated (Figure 2), and the spatial overlaps were reasonably comparable, regardless of the imaging method (Figures 4–7).

The source of the OICa^{2+} signal is due to transient increases in cytosolic calcium, directly related to spiking activity (Wachowiak et al., 2013; Yaksi and Friedrich, 2006) (Supplementary Figure 1). Spiking activity is highly correlated with measured cytosolic calcium, blood flow, and glutamate release at the glomeruli during odor stimulation (Petzold et al., 2008). Other studies using intrinsic optical imaging reported that local metabolic coupling and blood flow were independent of post-synaptic activation during odor stimulation (Gurden et al., 2006). Furthermore, Gurden studies suggested that pre-synaptic glutamate release and uptake by astrocytes form critical pathways through which neural activity is linked to metabolic processing and hence functional hyperemic signals (Supplementary Figure 1). Petzold studies also showed calcium elevations in astrocytes and functional hyperemia depended on astrocytic metabotropic glutamate receptor 5 and cyclooxygenase activation. Both studies implicated the role of astrocytes in functional hyperemia during odor stimulation.

The BOLD response is based on energetic costs of the above-mentioned pre-synaptic events and post-synaptic dendritic integration (i.e., both inhibitory and excitatory potentials, Supplementary Figure 1), and is thus correlated with dynamics of local field potentials and multi-unit spiking activity for a variety of anesthetized and non-anesthetized conditions (Goense and Logothetis, 2008; Hirano et al., 2011; Logothetis et al., 2001; Maandag et al., 2007; Sanganahalli et al., 2009b; Smith et al., 2002). This is in agreement with numerous studies reporting strong correlations between pre-synaptic and fMRI or blood flow signals. Earlier studies attempted to simultaneously measure fMRI and calcium indicator signals using a fiber optics approach to investigate the relationship between BOLD and underlying neuronal activity (Schulz et al., 2012). Their findings highlight the complexity of BOLD signals, involving both neuronal and glial activity. The steps leading from neuronal or glial activity to hemodynamic changes are not completely understood. Even though the simultaneous measurement of BOLD and calcium signals in the study by Schulz is a novel and useful method, it is significantly limited in comparing the spatial activity patterns because the calcium imaging method they used was a single-fiber point measurement (1×1 pixel). In contrast, our wide-field optical imaging approach overcomes this limitation and allows comparison of the spatial activity patterns (256×256 pixels) of relative change in calcium activity across the whole dorsal OB to the patterns reported by fMRI. Here, both imaging modalities were performed on the same animal and the data were co-registered to the same space. There has been no other attempt thus far to carry out such a detailed comparison between these two mapping methods. Another novelty is that these methods are extremely complementary: whereas optical imaging can only study the dorsally activated

glomeruli at high spatio-temporal resolution, fMRI can measure the activity of the whole bulb with near glomerular spatial resolution.

Other studies have correlated functional hemodynamics with spiking activity of principal output neurons (Rees et al., 2000), local synaptic processing (Lauritzen, 2001), or combination of the two (Mukamel et al., 2005; Sanganahalli et al., 2009b). Earlier studies also recorded multi-unit activity of olfactory sensory neurons and presynaptic synaptopHluorin (spH) fluorescence from glomeruli in mice that express spH under control of the olfactory marker protein promoter (OMP) (Bozza et al., 2004). They observed a linear monotonic relation between spH fluorescence and the integrated olfactory nerve spike rate, indicating that OMP-spH fluorescence can be used as a marker of pre-synaptic activity over a wide dynamic range of physiological stimuli. The same group later measured simultaneous blood flow and pre-synaptic activity in olfactory glomeruli in vivo using multi-photon imaging. They found that pre-synaptic activity in glomeruli was highly correlated with functional hyperemia, and that arteriolar tone and local capillary perfusion were regulated by astrocytes. These results are in accord with our findings here. They concluded that astrocytes may also contribute to the high temporal and spatial correlation of blood flow increase and glucose consumption observed in functional brain imaging (Gurden et al., 2006; Petzold et al., 2008).

The results from the present study provide a multi-modal imaging perspective to further probe the complex mechanisms of glomerular activities (Supplementary Figure 1) - spanning from chemical, electrical, and metabolic activity at the neuropil which together support odor information processing in the OB system. Since it is acknowledged that energy consumption is a crucial factor that constrains neural function (Hyder et al., 2013; Karbowski, 2014), the fMRI method has been calibrated to determine the energy demand of the BOLD response (Hoge, 2012; Hyder and Rothman, 2012). We, however, agree that we cannot rule out that the post-synaptic response by itself could also have contributed to the BOLD image, as this is technically unfeasible using odorant perturbations only. Future calibrated fMRI studies of the OB, in conjunction with various agonists or antagonists, can be designed to assess whether the energy demands of pre- and post-synaptic activities track the glomerular input as imaged by OICa^{2+}. If glomerular input is found to match glomerular energy demand, then glomerular-level mapping by calibrated fMRI could allow quantitative odor mapping of the OB.

5. CONCLUSION

In summary, multi-modal functional imaging of the rat OB provides new insights into the complexities of neuropil activities. While wide-field OICa^{2+} may be used to feature the fast timing of dorsal glomerular clusters, fMRI may be used to map the entire glomerular sheet in the OB.

Supplementary Material

Refer to Web version on PubMed Central for supplementary material.

Acknowledgments

Supported by NIH grants R01 DC-011286 (to JVV and FH), R01 MH-067528 (to FH), and P30 NS-052519 (to FH). The authors thank colleagues at MRRC, especially Christoph Juchem for shimming methods and Bei Wang for surgical support.

References

Belluscio L, Katz LC. Symmetry, stereotypy, and topography of odorant representations in mouse olfactory bulbs. J Neurosci. 2001; 21:2113–2122. [PubMed: 11245695]

Bojsen-Moller F, Fahrenkrug J. Nasal swell-bodies and cyclic changes in the air passage of the rat and rabbit nose. J Anat. 1971; 110:25–37. [PubMed: 4110864]

Bozza T, McGann JP, Mombaerts P, Wachowiak M. In vivo imaging of neuronal activity by targeted expression of a genetically encoded probe in the mouse. Neuron. 2004; 42:9–21. [PubMed: 15066261]

Chaigneau E, Tiret P, Lecoq J, Ducros M, Knopfel T, Charpak S. The relationship between blood flow and neuronal activity in the rodent olfactory bulb. J Neurosci. 2007; 27:6452–6460. [PubMed: 17567806]

Charpak S, Mertz J, Beaurepaire E, Moreaux L, Delaney K. Odor-evoked calcium signals in dendrites of rat mitral cells. Proc Natl Acad Sci U S A. 2001; 98:1230–1234. [PubMed: 11158622]

Friedrich RW, Korsching SI. Combinatorial and chemotopic odorant coding in the zebrafish olfactory bulb visualized by optical imaging. Neuron. 1997; 18:737–752. [PubMed: 9182799]

Gautam SH, Short SM, Verhagen JV. Retronasal odor concentration coding in glomeruli of the rat olfactory bulb. Front Integr Neurosci. 2014; 8:81. [PubMed: 25386123]

Gautam SH, Verhagen JV. Evidence that the sweetness of odors depends on experience in rats. Chem Senses. 2010; 35:767–776. [PubMed: 20702508]

Gautam SH, Verhagen JV. Direct behavioral evidence for retronasal olfaction in rats. PLoS One. 2012; 7:e44781. [PubMed: 22970305]

Goense JB, Logothetis NK. Neurophysiology of the BOLD fMRI signal in awake monkeys. Curr Biol. 2008; 18:631–640. [PubMed: 18439825]

Gurden H, Uchida N, Mainen ZF. Sensory-evoked intrinsic optical signals in the olfactory bulb are coupled to glutamate release and uptake. Neuron. 2006; 52:335–345. [PubMed: 17046695]

Guthrie KM, Gall CM. Odors increase Fos in olfactory bulb neurons including dopaminergic cells. Neuroreport. 1995; 6:2145–2149. discussion 2103. [PubMed: 8595190]

Guthrie KM, Holmes J, Leon M. Focal 2-DG uptake persists following olfactory bulb lesions. Brain Res Bull. 1995; 38:129–134. [PubMed: 7583337]

Hirano Y, Stefanovic B, Silva AC. Spatiotemporal evolution of the functional magnetic resonance imaging response to ultrashort stimuli. J Neurosci. 2011; 31:1440–1447. [PubMed: 21273428]

Hoge RD. Calibrated FMRI. NeuroImage. 2012; 62:930–937. [PubMed: 22369993]

Homma R, Baker BJ, Jin L, Garaschuk O, Konnerth A, Cohen LB, Zecevic D. Wide-field and two-photon imaging of brain activity with voltage- and calcium-sensitive dyes. Philos Trans R Soc Lond B Biol Sci. 2009; 364:2453–2467. [PubMed: 19651647]

Hyder F, Rothman DL. Quantitative fMRI and oxidative neuroenergetics. NeuroImage. 2012; 62:985–994. [PubMed: 22542993]

Hyder F, Rothman DL, Bennett MR. Cortical energy demands of signaling and nonsignaling components in brain are conserved across mammalian species and activity levels. Proc Natl Acad Sci U S A. 2013; 110:3549–3554. [PubMed: 23319606]

Johnson BA, Leon M. Modular representations of odorants in the glomerular layer of the rat olfactory bulb and the effects of stimulus concentration. J Comp Neurol. 2000; 422:496–509. [PubMed: 10861522]

Joshi A, Scheinost D, Okuda H, Belhachemi D, Murphy I, Staib LH, Papademetris X. Unified framework for development, deployment and robust testing of neuroimaging algorithms. Neuroinformatics. 2011; 9:69–84. [PubMed: 21249532]

Juchem C, Herman P, Sanganahalli BG, Brown PB, McIntyre S, Nixon TW, Green D, Hyder F, de Graaf RA. DYNAmic Multi-coIl TEchnique (DYNAMITE) shimming of the rat brain at 11.7 T. NMR Biomed. 2014; 27:897–906. [PubMed: 24839167]

Jukovskaya N, Tiret P, Lecoq J, Charpak S. What does local functional hyperemia tell about local neuronal activation? J Neurosci. 2011; 31:1579–1582. [PubMed: 21289165]

Karbowski J. Constancy and trade-offs in the neuroanatomical and metabolic design of the cerebral cortex. Front Neural Circuits. 2014; 8:9. [PubMed: 24574975]

Kauer JS. Contributions of topography and parallel processing to odor coding in the vertebrate olfactory pathway. Trends Neurosci. 1991; 14:79–85. [PubMed: 1708541]

Kida I, Xu F, Shulman RG, Hyder F. Mapping at glomerular resolution: fMRI of rat olfactory bulb. Magn Reson Med. 2002; 48:570–576. [PubMed: 12210928]

Kikuta S, Kashiwadani H, Mori K. Compensatory rapid switching of binasal inputs in the olfactory cortex. J Neurosci. 2008; 28:11989–11997. [PubMed: 19005064]

Lam YW, Cohen LB, Wachowiak M, Zochowski MR. Odors elicit three different oscillations in the turtle olfactory bulb. J Neurosci. 2000; 20:749–762. [PubMed: 10632604]

Lauritzen M. Relationship of spikes, synaptic activity, and local changes of cerebral blood flow. J Cereb Blood Flow Metab. 2001; 21:1367–1383. [PubMed: 11740198]

Li B, Gong L, Wu R, Li A, Xu F. Complex relationship between BOLD-fMRI and electrophysiological signals in different olfactory bulb layers. NeuroImage. 2014; 95:29–38. [PubMed: 24675646]

Logothetis NK, Pauls J, Augath M, Trinath T, Oeltermann A. Neurophysiological investigation of the basis of the fMRI signal. Nature. 2001; 412:150–157. [PubMed: 11449264]

Maandag NJ, Coman D, Sanganahalli BG, Herman P, Smith AJ, Blumenfeld H, Shulman RG, Hyder F. Energetics of neuronal signaling and fMRI activity. Proc Natl Acad Sci U S A. 2007; 104:20546–20551. [PubMed: 18079290]

Moreaux L, Laurent G. Estimating firing rates from calcium signals in locust projection neurons in vivo. Front Neural Circuits. 2007; 1:2. [PubMed: 18946544]

Mukamel R, Gelbard H, Arieli A, Hasson U, Fried I, Malach R. Coupling between neuronal firing, field potentials, and FMRI in human auditory cortex. Science. 2005; 309:951–954. [PubMed: 16081741]

Nawroth JC, Greer CA, Chen WR, Laughlin SB, Shepherd GM. An energy budget for the olfactory glomerulus. J Neurosci. 2007; 27:9790–9800. [PubMed: 17804639]

Osmanski BF, Martin C, Montaldo G, Laniece P, Pain F, Tanter M, Gurden H. Functional ultrasound imaging reveals different odor-evoked patterns of vascular activity in the main olfactory bulb and the anterior piriform cortex. NeuroImage. 2014; 95:176–184. [PubMed: 24675645]

Petzold GC, Albeanu DF, Sato TF, Murthy VN. Coupling of neural activity to blood flow in olfactory glomeruli is mediated by astrocytic pathways. Neuron. 2008; 58:897–910. [PubMed: 18579080]

Poplawsky AJ, Kim SG. Layer-dependent BOLD and CBV-weighted fMRI responses in the rat olfactory bulb. NeuroImage. 2014; 91:237–251. [PubMed: 24418506]

Qureshy A, Kawashima R, Imran MB, Sugiura M, Goto R, Okada K, Inoue K, Itoh M, Schormann T, Zilles K, Fukuda H. Functional mapping of human brain in olfactory processing: a PET study. J Neurophysiol. 2000; 84:1656–1666. [PubMed: 10980035]

Ratzlaff EH, Grinvald A. A tandem-lens epifluorescence macroscope: hundred-fold brightness advantage for wide-field imaging. J Neurosci Methods. 1991; 36:127–137. [PubMed: 1905769]

Rees G, Friston K, Koch C. A direct quantitative relationship between the functional properties of human and macaque V5. Nat Neurosci. 2000; 3:716–723. [PubMed: 10862705]

Rubin BD, Katz LC. Optical imaging of odorant representations in the mammalian olfactory bulb. Neuron. 1999; 23:499–511. [PubMed: 10433262]

Sanganahalli BG, Bailey CJ, Herman P, Hyder F. Tactile and non-tactile sensory paradigms for fMRI and neurophysiologic studies in rodents. Methods Mol Biol. 2009a; 489:213–242. [PubMed: 18839094]

Sanganahalli BG, Herman P, Blumenfeld H, Hyder F. Oxidative neuroenergetics in event-related paradigms. J Neurosci. 2009b; 29:1707–1718. [PubMed: 19211878]

Schafer JR, Kida I, Rothman DL, Hyder F, Xu F. Adaptation in the rodent olfactory bulb measured by fMRI. Magn Reson Med. 2005; 54:443–448. [PubMed: 16032685]

Schafer JR, Kida I, Xu F, Rothman DL, Hyder F. Reproducibility of odor maps by fMRI in rodents. NeuroImage. 2006; 31:1238–1246. [PubMed: 16632382]

Schulz K, Sydekum E, Krueppel R, Engelbrecht CJ, Schlegel F, Schroter A, Rudin M, Helmchen F. Simultaneous BOLD fMRI and fiber-optic calcium recording in rat neocortex. Nat Methods. 2012; 9:597–602. [PubMed: 22561989]

Sharp FR, Kauer JS, Shepherd GM. Local sites of activity-related glucose metabolism in rat olfactory bulb during olfactory stimulation. Brain Res. 1975; 98:596–600. [PubMed: 1182541]

Smith AJ, Blumenfeld H, Behar KL, Rothman DL, Shulman RG, Hyder F. Cerebral energetics and spiking frequency: the neurophysiological basis of fMRI. Proc Natl Acad Sci U S A. 2002; 99:10765–10770. [PubMed: 12134056]

Stewart WB, Kauer JS, Shepherd GM. Functional organization of rat olfactory bulb analysed by the 2-deoxyglucose method. J Comp Neurol. 1979; 185:715–734. [PubMed: 447878]

Uchida N, Takahashi YK, Tanifuji M, Mori K. Odor maps in the mammalian olfactory bulb: domain organization and odorant structural features. Nat Neurosci. 2000; 3:1035–1043. [PubMed: 11017177]

Verhagen JV, Wesson DW, Netoff TI, White JA, Wachowiak M. Sniffing controls an adaptive filter of sensory input to the olfactory bulb. Nat Neurosci. 2007; 10:631–639. [PubMed: 17450136]

Wachowiak M, Cohen LB. Presynaptic afferent inhibition of lobster olfactory receptor cells: reduced action-potential propagation into axon terminals. J Neurophysiol. 1998; 80:1011–1015. [PubMed: 9705490]

Wachowiak M, Cohen LB. Representation of odorants by receptor neuron input to the mouse olfactory bulb. Neuron. 2001; 32:723–735. [PubMed: 11719211]

Wachowiak M, Cohen LB. Correspondence between odorant-evoked patterns of receptor neuron input and intrinsic optical signals in the mouse olfactory bulb. J Neurophysiol. 2003; 89:1623–1639. [PubMed: 12612023]

Wachowiak M, Cohen LB, Ache BW. Presynaptic inhibition of olfactory receptor neurons in crustaceans. Microsc Res Tech. 2002a; 58:365–375. [PubMed: 12214303]

Wachowiak M, Cohen LB, Zochowski MR. Distributed and concentration-invariant spatial representations of odorants by receptor neuron input to the turtle olfactory bulb. J Neurophysiol. 2002b; 87:1035–1045. [PubMed: 11826067]

Wachowiak M, Economo MN, Diaz-Quesada M, Brunert D, Wesson DW, White JA, Rothermel M. Optical dissection of odor information processing in vivo using GCaMPs expressed in specified cell types of the olfactory bulb. J Neurosci. 2013; 33:5285–5300. [PubMed: 23516293]

Xu F, Kida I, Hyder F, Shulman RG. Assessment and discrimination of odor stimuli in rat olfactory bulb by dynamic functional MRI. Proc Natl Acad Sci U S A. 2000; 97:10601–10606. [PubMed: 10973488]

Xu F, Liu N, Kida I, Rothman DL, Hyder F, Shepherd GM. Odor maps of aldehydes and esters revealed by functional MRI in the glomerular layer of the mouse olfactory bulb. Proc Natl Acad Sci U S A. 2003; 100:11029–11034. [PubMed: 12963819]

Yaksi E, Friedrich RW. Reconstruction of firing rate changes across neuronal populations by temporally deconvolved Ca2+ imaging. Nat Methods. 2006; 3:377–383. [PubMed: 16628208]

Yang X, Renken R, Hyder F, Siddeek M, Greer CA, Shepherd GM, Shulman RG. Dynamic mapping at the laminar level of odor-elicited responses in rat olfactory bulb by functional MRI. Proc Natl Acad Sci U S A. 1998; 95:7715–7720. [PubMed: 9636216]

Youngentob SL, Mozell MM, Sheehe PR, Hornung DE. A quantitative analysis of sniffing strategies in rats performing odor detection tasks. Physiol Behav. 1987; 41:59–69. [PubMed: 3685154]

Highlights

- We succeeded in concurrent imaging of same rats with fMRI and wide-field calcium imaging for orthonasal odor stimuli.
- Excellent correspondence between odor-evoked fMRI and calcium imaging maps was observed.
- Odor-specific glomerular patterns by fMRI primarily tracks pre-synaptic input to the olfactory bulb.

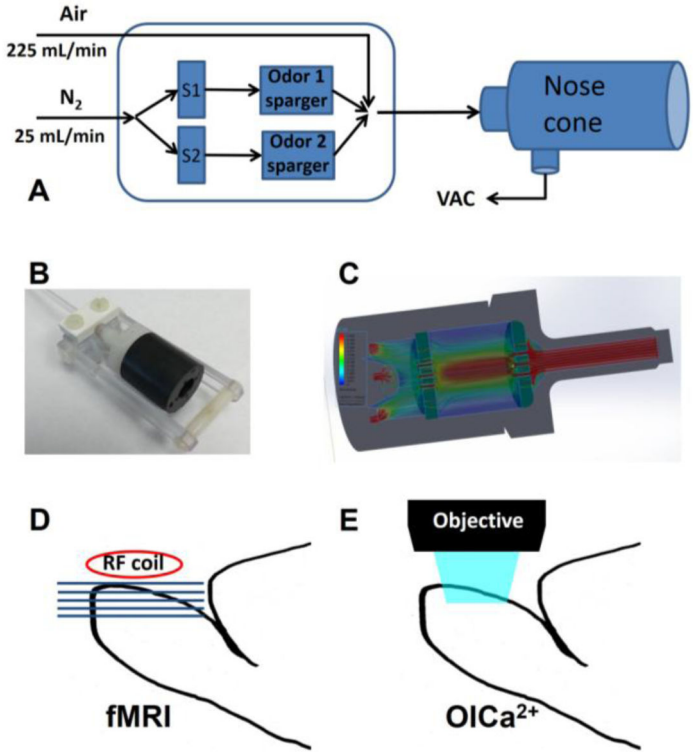

Figure 1.

Schematic of odor stimulation for fMRI and $OICa^{2+}$ experiments. (**A**) A custom-built odor delivery system was used to present the different odor stimuli to the nose of rats. Air continuously blew through the system at 225 mL/min while during stimulation computer controlled solenoid valves (S1 or S2) allowed N_2 flow (25 mL/min) through odor spargers. After stimulation a vacuum line removed the excess odor from the nose cone. (**B**) A specially designed nose cone, mounted to the naso-incisor bite bar, delivered the odorant from a connecting Teflon tube to both nares in widened laminar flow. (**C**) The nose cone design was based on flow simulation in SolidWorks. (**D**) During fMRI recording the rat was positioned prone in a specially designed plastic holder in such manner that a surface coil (diameter, 1.4 cm) was at the top of the rat's OB allowing axially oriented slices. (**E**) During $OICa^{2+}$ recording the rat was also positioned prone, but the objective was positioned above the dorsal OB and images were recorded through a transparent closed cranial window.

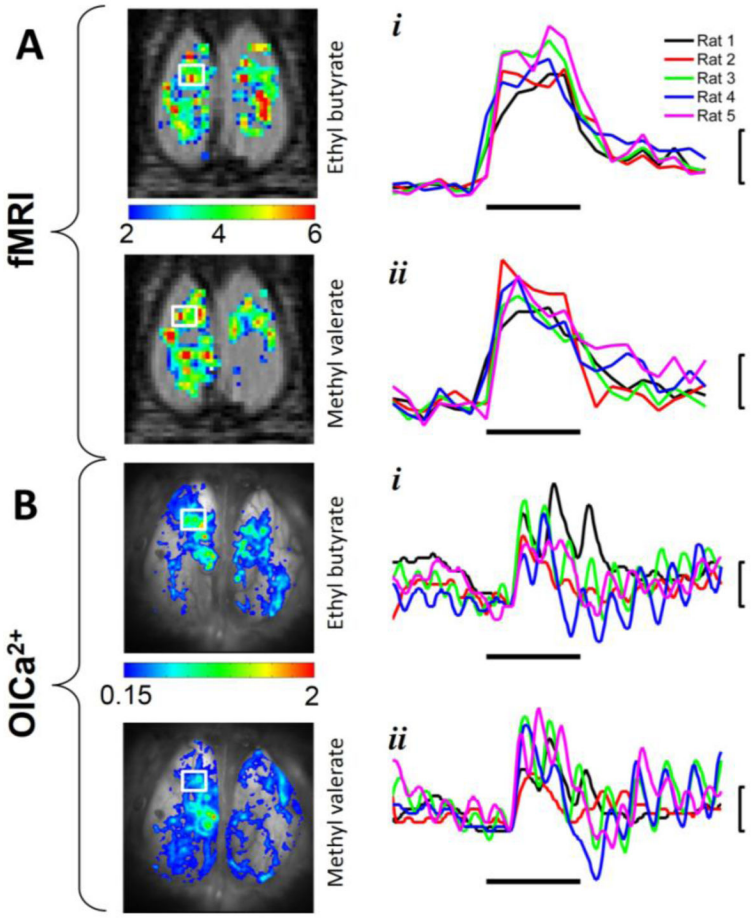

Figure 2.

Comparison of fMRI and OICa^{2+} data from the same subject (Rat 1). Single trial activation maps for **(A)** fMRI and **(B)** OICa^{2+} are shown from the same subject in original space for each modality, where the time courses were extracted from the ROIs (indicated by the white box on the left OB) for **(i)** EB and **(ii)** MV. The odor exposure periods are indicated by the horizontal bars, which were 2 minutes and 2 seconds for **(A)** fMRI and **(B)** OICa^{2+}, respectively. The response magnitudes are indicated by the vertical bars, which were 4% and 1% for **(A)** fMRI and **(B)** OICa^{2+}, respectively. All traces in **B** were band pass filtered (0.2–4 Hz), where the fluctuation caused by breathing is visible on all OICa^{2+} traces. The different colored traces in **A** and **B** represent all rats imaged by both modalities.

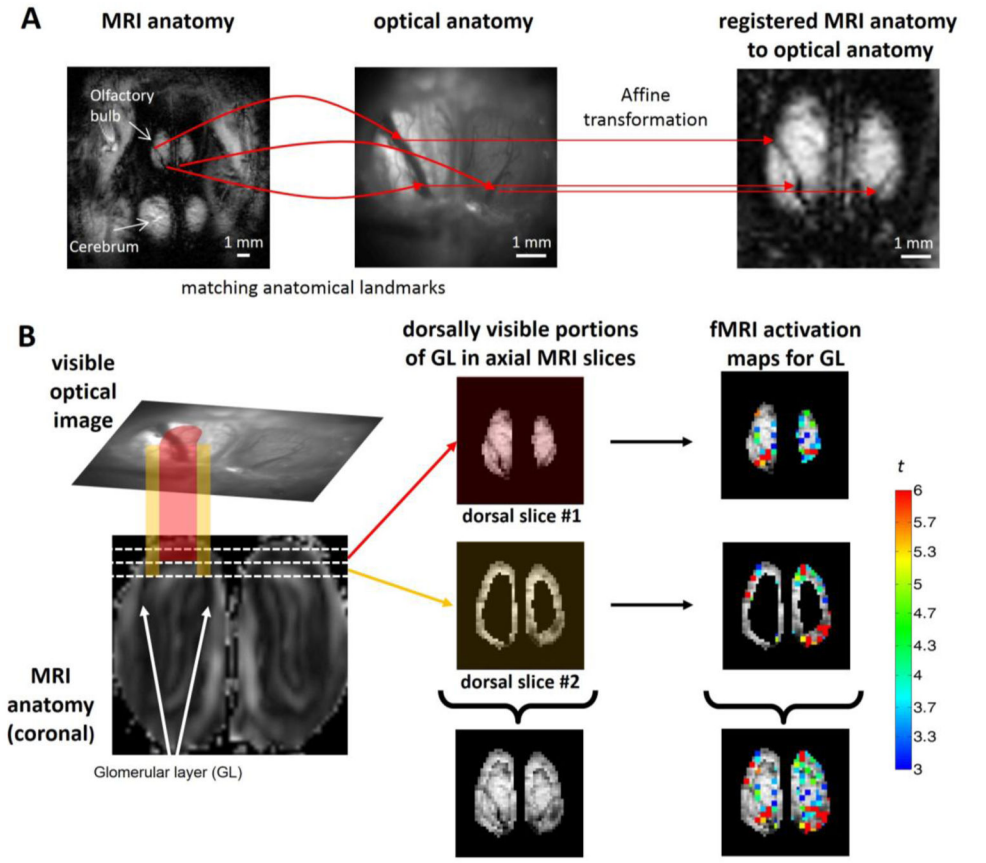

Figure 3.

Registering fMRI data onto OICa^{2+} space. **(A)** Co-registration is based on identical anatomical points of the MRI anatomical image (left panel, FOV = 15.6×15.6 mm, in-plane resolution = 128×128 pixels) and the optical anatomical image (middle panel, FOV = 6.7×6.7 mm, in-plane resolution = 256×256 pixels) using the vessel structure of the OB (curved red arrows). The calculated affine transformation matrix registered the MRI anatomical image to the optical space (right panel), where the identical points have the same coordinates in both images (straight red arrows from the middle panel to the right panel). **(B)** The fMRI data are sectioned images (i.e. horizontal cross-sections of the 3D OB is visualized as 2D images) while OICa^{2+} data are projective images (i.e., the dorsal portion of the 3D OB is projected as a 2D image, top part of the left panel). Consequently the visible optical image shows details of the OB that are not only described by the upper dorsal MRI image (red projection, top part of middle panel), but also partly by the second dorsal MRI image as well (orange projection, middle part of the middle panel). The white lines on the coronal MRI image (bottom part of left panel) show the cross-sections of the 300 μm thick axial MRI images. The upper axial MRI slice (shown with reddish hue) is completely visible from the upper point of view in the optical image, but in addition the edge of the second dorsal MRI slice (shown with orange hue) is also visible from above in the optical image. Thus these sections of the MRI images when combined represent a close approximate of the projective image of the OB in optical space (bottom part of the middle panel). Applying this method for BOLD activation maps (Student's t-test statistic is shown in color in the right

panel) we created the summed fMRI activation map (bottom part of the right panel) that was registered and directly compared to the OICa^{2+} images (see Figure 4). The data shown here are from Rat 3.

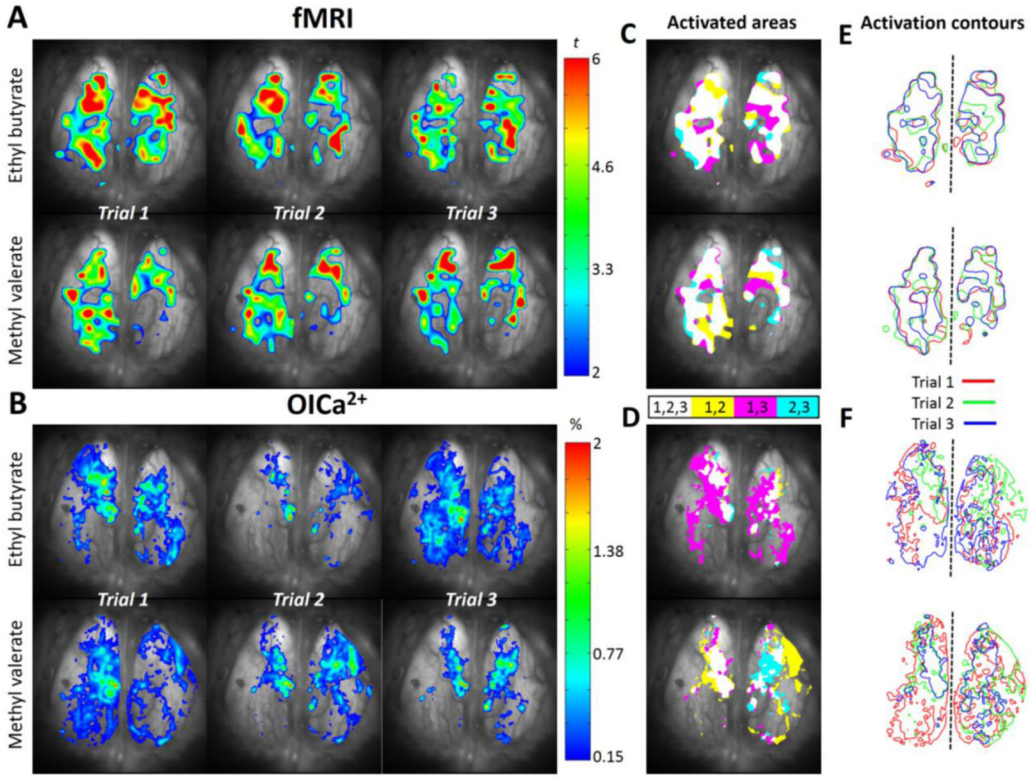

Figure 4.

Reproducibility of fMRI and OICa^{2+} activated areas from the same subject (Rat 1). **(A)** Odor-induced BOLD activations are shown as Student'-t maps across 3 trials for EB and MV with colors indicating t-statistics ranging from 2 to 6. **(B)** Odor-induced Ca^{2+} activation maps are calculated as percentage change of fluorescent intensity (0.15–2%) across 3 trials for EB and MV. **(C, D)** The areas of activation trial-by-trial are converted to binary values and represented as color patterns showing only those areas where at least two stimulations overlap, i.e., white (activation in trails 1, 2, 3), yellow (activation in trials 1, 2), pink (activation areas in trials 1, 3), and indigo (activation areas in trials 1, 2) color. **(E, F)** The contour maps of the activated areas across trials (red, blue, and green lines, for trials 1–3) show the overlap of activated area, where dashed line separates left and right OBs.

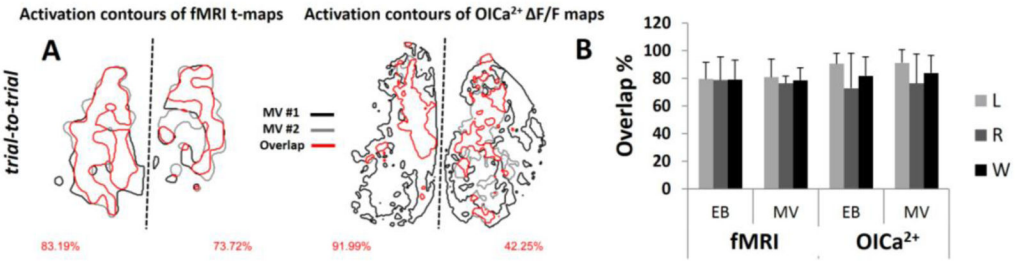

Figure 5.

Trial-to-trial comparison of activated areas with fMRI and OICa^{2+}. **(A)** The red contour line shows the overlap between activated areas with two stimulations (black and gray contours) for the same odor (i.e., MV across two trials) for fMRI and OICa^{2+} for the same subject (see Figure 4). The percent of activation overlaps are on the bottom left and right corners for left and right OBs. **(B)** The statistics of the activation overlaps within measuring modalities for every experiment are shown as mean and SD. The left (L), right (R) and the whole (W) OB data are shown. For MV, the overlaps were 80.9±13.1%, 76.3±5.24%, 78.6±8.9% with fMRI and 91.3±9.4%, 76.3±21.3%, 88.8±12.7% with OICa^{2+}. For EB, the overlaps were 79.5±12.1%, 78.7±16.8%, 79.1±14.1% with fMRI and 90.6±7.6%, 72.9±25.1%, 81.7±13.6% with OICa^{2+}.

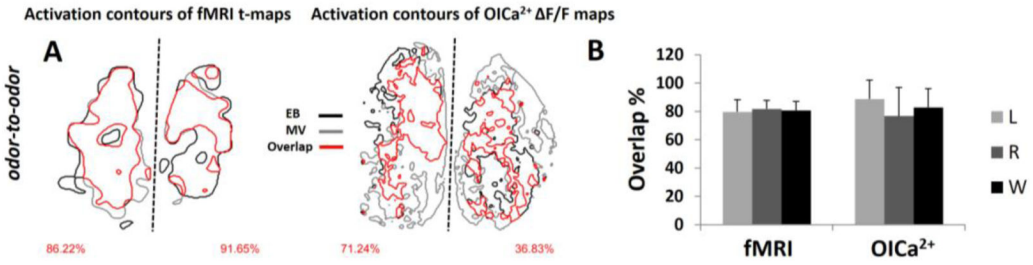

Figure 6.

Odor-to-odor comparison of activated areas with fMRI and OICa^{2+}. **(A)** The red contour line show the overlap between activated areas for the two odors (EB and MV) are shown by black and gray contours, respectively) odors for fMRI and OICa^{2+} for the same subject (see Figure 4). The percent of activation overlaps are on the bottom left and right corners for left and right OBs. **(B)** The statistics of the activation overlaps within measuring modalities for every experiment are shown as mean and SD. The left (L), right (R) and the whole (W) OB data are shown. Inter-odor overlaps in left, right, and whole OB, across all 5 rats, were 79.6±8.7%, 81.7±6.0%, 80.7±6.3% for fMRI and 88.7±13.4%, 76.7±20.3%, 82.7±13.6% for OICa^{2+}.

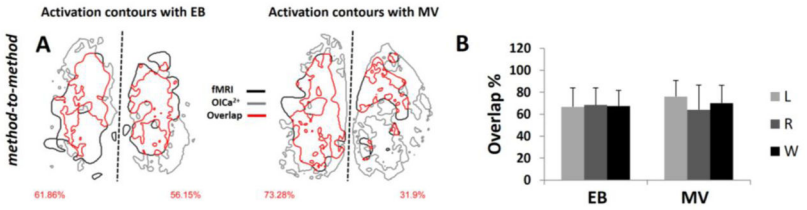

Figure 7.

Method-to-method comparison of activated areas with fMRI and OICa^{2+}. **(A)** The red contour line shows the overlap between activated areas (fMRI and OICa^{2+} indicated with black and gray contours, respectively) for EB and MV odor stimulations in the same subject (see Figure 4). The percent of activation overlaps are on the bottom left and right corners for left and right OBs. **(B)** The statistics of the activation overlaps for every experiment between methods are shown as mean and SD. The left (L), right (R) and the whole (W) OB data are shown. Inter-method overlaps in left, right, and whole OB, across all 5 rats, were 66.7±17.4%, 68.5±15.5%, 67.6±14.0% for EB and 76.1±14.5%, 64.1±22.4%, 70.1±16.3% for MV.